

Testing phenomenological and theoretical models of dark matter density profiles with galaxy clusters

Leandro J. Beraldo e Silva^{1,2,3*}, Marcos Lima^{1†} and Laerte Sodré Jr.^{4‡}

¹ Departamento de Física Matemática, Instituto de Física, Universidade de São Paulo, São Paulo SP, Brazil

² Institut d'Astrophysique de Paris, Paris, France

³ CAPES Foundation, Ministry of Education of Brazil, Brasília - DF 70.040-020, Brazil

⁴ Departamento de Astronomia, Instituto de Astronomia, Geofísica e Ciências Atmosféricas, Universidade de São Paulo, São Paulo SP, Brazil

ABSTRACT

We use the stacked gravitational lensing mass profile of four high-mass ($M \gtrsim 10^{15} M_{\odot}$) galaxy clusters around $z \approx 0.3$ from Umetsu et al. to fit density profiles of phenomenological [Navarro-Frenk-White (NFW), Einasto, Sérsic, Stadel, Baltz-Marshall-Oguri (BMO) and Hernquist] and theoretical (non-singular Isothermal Sphere, DARKexp and Kang & He) models of the dark matter distribution. We account for large-scale structure effects, including a 2-halo term in the analysis. We find that the BMO model provides the best fit to the data as measured by the reduced χ^2 . It is followed by the Stadel profile, the generalized NFW profile with a free inner slope and by the Einasto profile. The NFW model provides the best fit if we neglect the 2-halo term, in agreement with results from Umetsu et al. Among the theoretical profiles, the DARKexp model with a single form parameter has the best performance, very close to that of the BMO profile. This may indicate a connection between this theoretical model and the phenomenology of dark matter halos, shedding light on the dynamical basis of empirical profiles which emerge from numerical simulations.

Key words: cosmology: dark matter; galaxies: clusters; galaxies: halos

1 INTRODUCTION

Evidence for the existence of dark matter dates back to Zwicky (1933) with studies of the kinematics of galaxies in the Coma Cluster, which required the presence of a massive, smooth and dark component generating the cluster gravitational potential. More recently, astrophysical and cosmological observations as well as simulations and theoretical arguments have provided further indication for the existence of dark matter, and hopes that it may be detected directly in particle accelerators (see for example Frandsen et al. 2012, and references therein). These developments include the flatness of galaxy rotation curves (e.g., Bosma 1978; Bosma & van der Kruit 1979; Rubin, Thonnard & Ford 1978; Rubin, Ford & Thonnard 1980), the mass of galaxy clusters inferred either by their X-ray emission (e.g., Allen, Schmidt & Fabian 2002) and Vikhlinin et al. (2006) or by gravitational lensing (e.g. Clowe et al. 2006; Umetsu et al. 2011b; Mira et al. 2011), the acoustic oscillations measured in the cosmic microwave background (see WMAP papers, e.g. Jarosik et al. 2011) and in galaxy surveys (e.g. Eisenstein et al. 2005; Sánchez et al. 2012), and detailed studies of structure forma-

tion on numerical simulations with ever increasing precision (e.g. Springel et al. 2005; Alimi et al. 2012).

In the standard scenario, dark matter is assumed to be composed of particles that interact gravitationally but not electromagnetically. Within this picture, simulations of structure formation have shown a number of interesting results regarding the final states of systems of gravitationally interacting particles. For example, it has been shown that dark matter is cold, i.e. its particles must have had non-relativistic velocities around the epoch of recombination, otherwise structures like galaxies and galaxy clusters would be more diffuse than they appear due to free-streaming.

Another feature that emerges from simulations, and is confirmed by observations, is that these systems seem to achieve a final state of equilibrium, displaying nearly *universal* density profiles $\rho(r)$ (Navarro, Frenk & White 1996, 1997) and pseudo phase-space profiles $\rho(r)/\sigma^3(r)$ (Taylor & Navarro 2001) where $\sigma(r)$ is either the radial or total velocity dispersion. This is intriguing because these non-collisional systems interact only through gravitational effects, making them quite different from e.g. a molecular gas in a box. We are then led to approach the question of how a non-collisional process could bring a gravitational system to an equilibrium state in a time scale of the age of the Universe.

In an attempt to answer this kind of question, Lynden-Bell (1967) developed the mechanism of violent relaxation, in which the system's constituents, e.g. stars or dark matter particles, interact mainly with a time-varying average gravitational field, for which

* E-mail: lberaldo@if.usp.br

† E-mail: mlima@fma.if.usp.br

‡ E-mail: laerte@astro.iag.usp.br

the time scale to achieve an equilibrium state is many orders of magnitude smaller than that of two-particle interactions. However there are issues in this approach, like infinite masses and mass segregation. These happen because the model generates density profiles similar to that of an Isothermal Sphere (see below). For more details on these and other critics to the Lynden-Bell (1967) approach, see e.g. Hjorth & Williams (2010) and references therein.

Regardless of the discussions about the statistical process involved, the density profiles provided by simulations are observed in real objects like galaxy clusters, in which the role of the baryonic component is relatively small compared to that of dark matter. Phenomenologically, one can argue that if simulations provide density profiles which match those in observed data, that means that the assumptions made in the simulations are likely correct, and the observed features are consequences of the gravitational interaction. Nonetheless, a deeper understanding of the physical mechanisms that lead to equilibrium in gravitational systems is certainly desirable. In fact, ignoring this issue would be equivalent to making simulations of a molecular gas in a box and computing gas pressure and velocity distribution from the simulated results, with no regards to the kinetic gas theory developed by Maxwell, Boltzmann and others.

In order to have a better dynamical picture of gravitational systems in general, and of dark matter halos in particular, first principle models have been developed to explain the features seen in simulations and observations. In particular, there has been a great effort to make predictions of the three-dimensional density profile $\rho(\mathbf{r})$ of dark matter halos. The connection with observations is made via the surface density profile $\Sigma(R)$ projected in the line-of-sight x_{\parallel}

$$\Sigma(R) = \int dx_{\parallel} \rho(x_{\parallel}, R), \quad (1)$$

where $\mathbf{r} = (x_{\parallel}, R)$ and R is the projected distance on the plane of the sky. Compared to galaxies, for which dissipative effects of cold baryons are important, galaxy clusters are excellent to test the distribution of dark matter, because in clusters most of the baryons are hot and dissipate less. Thus, the total density profile, inferred e.g. from gravitational lensing measurements, provides reliable information about the dark matter density profile. In fact, lensing is particularly interesting in the determination of the observed density profile of galaxy clusters, because it does not require assumptions of hydrostatic equilibrium, as in dynamical methods.

In this paper we use the stacked surface density profile from four massive galaxy clusters with similar mass and redshift to test both phenomenological and theoretical models for their density profiles. We only consider spherically symmetrical models. In §2 we briefly describe the cluster data used in this work. In §3 and §4 we present the phenomenological and theoretically motivated models tested. In §5 we present the halo model, which allows us to include large-scale structure effects on the observed profiles. Our results are presented in §6 and discussed in §7. When necessary, we use for the cosmological parameters: $\Omega_m = 0.275$ and $\Omega_{\Lambda} = 0.725$.

2 DATA

We use the data of Umetsu et al. (2011b), who combined weak-lensing shear, magnification, and strong-lensing measurements of four high-mass ($M \gtrsim 10^{15} M_{\odot}$) galaxy clusters (A1689, A1703, A370, C10024+17) with redshifts around $z \approx 0.3$. The strong lensing data was based on Hubble Space Telescope observations for the central regions of those clusters (typically, $R \lesssim 150 \text{ kpc}/h$),

Cluster	Redshift	r_{vir} ($Mpc h^{-1}$)	M_{vir} ($10^{15} M_{\odot} h^{-1}$)
A1689	0.183	2.011 ± 0.113	1.300 ± 0.205
A1703	0.281	1.915 ± 0.148	1.325 ± 0.221
A370	0.375	2.215 ± 0.079	2.399 ± 0.249
C10024+17	0.395	1.799 ± 0.105	1.329 ± 0.224

Table 1. Properties of individual clusters: name, redshift, virial radius and virial mass. Data extracted from Tables (1) and (7) of Umetsu et al. (2011a).

and combined with independent weak-lensing data obtained by Umetsu et al. (2011a), extending to the outer regions ($R \lesssim 3.5 \text{ Mpc}/h$) of the clusters.

The uncertainties and covariance matrices on the individual surface density profiles were calculated by Umetsu et al. (2011b) taking into account the observational errors as well as “the effect of uncorrelated large scale structure projected along the line of sight”, which can be determined once a cosmological model is assumed. The virial radii and virial masses were obtained using the non-parametric deprojection method developed by Broadhurst & Barkana (2008). A summary of the properties of the individual clusters is shown in Table (1) (data from Umetsu et al. 2011a).

In order to have an averaged cluster representative of the sample, also reducing the cosmic noise and smoothing effects due to asphericity or presence of substructures, Umetsu et al. (2011b) built a stacked surface density profile, scaling the individual cluster profiles by their virial radii. This procedure is justified given the narrow range in redshift and mass of the individual clusters [see Table (1)]. It also takes into account the different redshifts and their corresponding weight in the calculation of the full covariance matrix V_{ij} .

Hereafter we assume that the radial shape of the mean density profile obtained in this way is representative of dark matter halos in equilibrium (Gao et al. 2012). For more detailed information about the observations, uncertainties and stacking process, see Umetsu et al. (2011b).

3 PHENOMENOLOGICAL MODELS

A number of phenomenological models for density profiles of dark matter halos and galaxy clusters have been proposed as parametrized functions that fit reasonably well simulations and observations, with no regards to fundamental principles or theoretical motivation. Below we make a brief description of the models that we test.

3.1 NFW profile

The NFW profile was proposed by Navarro, Frenk & White (1996, 1997) in order to fit the data of N-body cold dark matter (CDM) simulations, after stacking many halos. It is given by

$$\rho(r) = \frac{\rho_s}{(r/r_s)(1+r/r_s)^2}, \quad (2)$$

where ρ_s and r_s are scale parameters. It often represents the best fit model to observed data of galaxy clusters; this would also be the case in this work if we did not include large-scale structure effects

in the analysis, as discussed below. The NFW profile has an analytical expression for the surface density profile $\Sigma(R)$ (Bartelmann 1996), given by

$$\Sigma(R) = 2\rho_s r_s F(R/r_s), \quad (3)$$

where

$$F(X) = \begin{cases} \frac{1}{X^2-1} \left(1 - \frac{2}{\sqrt{1-X^2}} \operatorname{arctanh} \sqrt{\frac{1-X}{1+X}} \right), & (X < 1) \\ \frac{1}{3}, & (X = 1) \\ \frac{1}{X^2-1} \left(1 - \frac{2}{\sqrt{X^2-1}} \operatorname{arctan} \sqrt{\frac{X-1}{X+1}} \right). & (X > 1) \end{cases}$$

The NFW profile has a non-physical divergence at the origin, varying as r^{-1} in the inner regions. In its outer parts it varies as r^{-3} , implying another unrealistic property of an infinite total mass. One way to circumvent the latter divergence is to truncate the profile at a maximum radius, e.g. the virial radius.

A common generalization of the NFW profile (Zhao 1996; Jing & Suto 2000) is obtained by setting the inner slope as a free parameter α (for NFW, $\alpha = -1$):

$$\rho(r) = \frac{\rho_s}{(r/r_s)^\alpha (1+r/r_s)^{3-\alpha}}, \quad (4)$$

Following Umetsu et al. (2011b) we will refer to this generalized model as gNFW.

3.2 BMO profile

Another useful modification of the NFW profile is that proposed by Baltz, Marshall & Oguri (2009), which incorporates a polynomial, smooth, truncation in the outer regions, obtaining a profile steeper than the NFW in this region. In this way, the problem with the infinite mass of NFW is circumvented and the influence of the 2-halo term can be better taken into account, as discussed in § 5. The function proposed has the following shape:

$$\rho(r) = \frac{\rho_s}{(r/r_s)(1+r/r_s)^2} \left(\frac{r_t^2}{r^2+r_t^2} \right)^n, \quad (5)$$

with n and r_t being free parameters. Actually, we obtained better results in the fits fixing $n = 2$.

3.3 Sérsic profile

The Sérsic profile (see Sérsic 1963) was proposed in order to fit the light distribution in spheroidal galaxies and has been also used to fit simulated data (Merritt et al. 2006). It is defined as a projected surface density profile that has the form

$$\Sigma(R) = \Sigma_e \exp \left\{ -b_n \left[(R/R_e)^{1/n} - 1 \right] \right\}, \quad (6)$$

where Σ_e is the surface brightness at the effective radius R_e and b_n is a function of n obtained by imposing that the luminosity inside the effective radius is half the total luminosity. The relation between b_n and n is well approximated by $b_n \approx 2n - 0.324$ (Ciotti 1991).

3.4 Einasto profile

The Einasto profile is a three-dimensional version of the Sérsic profile (see Einasto 1965). It was proposed to describe the surface

brightness of elliptical galaxies. Recently it has also been used to fit data from N-body CDM simulations, giving results comparable to the NFW profile in some cases (Navarro et al. 2004; Merritt et al. 2005, 2006; Gao et al. 2008; Navarro et al. 2010). It is given by

$$\rho(r) = \rho_s \exp \left\{ -2n \left[(r/r_{-2})^{1/n} - 1 \right] \right\}, \quad (7)$$

where ρ_s and r_{-2} are scale parameters. Lapi & Cavaliere (2011) discuss a possible dynamical basis that could generate a profile for which Einasto is a good approximation. In their Appendix A, Mamon, Biviano & Murante (2010) have obtained a polynomial approximation to better than 0.8% for the expression of the surface density, in the intervals $3.5 \leq n \leq 6.5$ and $-2 \leq \log_{10}(R/r_{-2}) \leq 2$.

3.5 Stadel profile

This profile was proposed to fit simulated data of galaxy-size dark matter halos (see Stadel et al. 2009). It has the form

$$\rho(r) = \rho_0 \exp \left\{ -\lambda [\ln(1+r/r_s)]^2 \right\}, \quad (8)$$

which resembles somewhat the Einasto profile and similarly gives a finite density ρ_0 at the origin. It can also be written as

$$\rho(r) = \frac{\rho_0}{(1+r/r_s)^{\lambda \ln(1+r/r_s)}}, \quad (9)$$

and in this way it resembles power-law profiles. Noticing that the shape parameter assumed almost the same value $\lambda = 0.1$ in different simulations, Stadel et al. (2009) proposed to fix this parameter and promote the model into a two-parameter profile. Here we let λ be a free parameter and obtain a different value for it.

3.6 Hernquist profile

The Hernquist (1990) profile has the functional form

$$\rho(r) = \frac{\rho_s}{(r/r_s)(1+r/r_s)^3}, \quad (10)$$

and differs from the NFW profile only in the outer parts, where it varies as r^{-4} . It was proposed, not as a fit to simulated or observed data, but because it provides analytical expressions for dynamical quantities, such as the gravitational potential, the energy distribution function, the density of states as well as the surface density, which is given by

$$\Sigma(R) = 2\rho_s r_s G(R/r_s), \quad (11)$$

where

$$G(X) = \frac{[(2+X^2)H(X) - 3]}{2(1-X^2)^2}, \quad (12)$$

and

$$H(X) = \begin{cases} \frac{1}{\sqrt{1-X^2}} \operatorname{sech}^{-1} X, & (X < 1) \\ 1, & (X = 1) \\ \frac{1}{\sqrt{X^2-1}} \operatorname{sec}^{-1} X, & (X > 1) \end{cases}$$

which implies that $\lim_{X \rightarrow 1} G(X) = 2/15$.

After addition of the 2-halo term explained in §5, the phenomenological profiles described above are shown in Fig. 2, along with the galaxy cluster stacked data from Umetsu et al. (2011b).

4 THEORETICAL MODELS

Some of the theoretical models we investigate here are based on the hypothesis of hydrostatic equilibrium between the gravitational attraction and the pressure $P(r)$ due to velocity dispersion in an isotropic distribution:

$$\frac{dP}{dr} = -\rho(r) \frac{GM(r)}{r^2}, \quad (13)$$

where $\rho(r)$ is the mass density profile and $M(r)$ is the total mass inside radius r :

$$M(r) = \int_0^r dr' 4\pi r'^2 \rho(r'). \quad (14)$$

Combining Eqs. (13) and (14) we have

$$\frac{d}{dr} \left[\frac{r^2}{\rho(r)} \frac{dP}{dr} \right] = -4\pi G r^2 \rho(r). \quad (15)$$

Choosing the equation of state $P(\rho)$ determines the model, and Eq. (15) can then be (numerically) solved to give the density profile $\rho(r)$.

4.1 (non-singular) Isothermal Sphere

The (non-singular) Isothermal Sphere is based on the equation of state of an ideal gas $P = nk_B T$, which locally becomes

$$P(r) = \frac{k_B T}{m} \rho(r), \quad (16)$$

where m is the mass of the constituent particle. Using Eq. (16) in Eq. (15) we have

$$r\rho \frac{d^2\rho}{dr^2} - r \left(\frac{d\rho}{dr} \right)^2 + 2\rho \frac{d\rho}{dr} + 4\pi G \lambda r \rho^3 = 0, \quad (17)$$

where $\lambda = m/k_B T$. This represents a particular case of the so-called Lane-Emden equation. The (non-singular) Isothermal Sphere has null slope at the origin and oscillates around the Singular Isothermal Sphere ($\rho \propto r^{-2}$) for large radii (Binney & Tremaine 2008). Thus we solve Eq. (17) numerically imposing the boundary conditions $d\rho/dr(0) = 0$ and $\rho(0) = \rho_0$, where ρ_0 is a free parameter.

4.2 Kang & He models

The entropy per unit mass s_r of an ideal gas, written as a function of pressure p_r and density profile $\rho(r)$ is

$$s_r = \ln \left(p_r^{3/2} \rho^{-5/2} \right), \quad (18)$$

and the Jeans equation is written as

$$\frac{dp_r}{dr} + 2\beta \frac{p_r}{r} = -\rho \frac{GM(r)}{r}, \quad (19)$$

where $\beta = 1 - (\sigma_\theta^2 + \sigma_\phi^2) / (2\sigma_r^2)$ is the velocity anisotropy parameter, written in terms of the velocity dispersions in the three spherical coordinates. Kang & He (2011) define a generalized pressure P as

$$\frac{dP}{dr} = \frac{dp_r}{dr} + 2\beta \frac{p_r}{r} \quad (20)$$

and a phenomenological entropy as

$$s = \ln \left(P^{3/2} \rho^{-5/2} \right), \quad (21)$$

such that the resulting system of equations is independent of β . This effectively reduces Eq. (19) to Eq. (13). Using the variational principle, the entropy per unit mass, Eq. (21), is then used to maximize the total entropy S

$$S = \int_0^\infty 4\pi r^2 \rho s dr = \int_0^\infty 4\pi r^2 \rho \ln \left(P^{3/2} \rho^{-5/2} \right) dr, \quad (22)$$

subject to the constraints of conservation of total energy and the virial theorem. This procedure results in the following equation of state

$$\rho = \lambda P + \mu P^\gamma, \quad (23)$$

where $\gamma = 3/5$. We will refer to this model as ‘‘Kang & He’’. The constant λ is a Lagrange multiplier and μ is an integration constant, both related to total mass and energy of the system. This equation of state reduces to that of an ideal gas Eq. (16) for $\mu = 0$ and $\lambda = m/k_B T$. Following a similar but different approach, Kang & He (2011) obtain the same equation, but now with $\gamma = 4/5$. We will call this last model ‘‘Kang & He 2’’.

In order to use the equation of state Eq. (23) in Eq. (15), we need to solve for $P(\rho)$ in Eq. (23), so as to turn Eq. (15) into an equation for $\rho(r)$. This is not possible for general values of γ , so after differentiating Eq. (23), Kang & He (2011) propose approximating $P \approx \rho/\lambda$, obtaining

$$\frac{dP}{dr} = \frac{1}{\lambda + \gamma\mu(\lambda/\rho)^{1-\gamma}} \frac{d\rho}{dr}. \quad (24)$$

Inserting Eq. (24) into Eq. (15), one obtains a second order differential equation for $\rho(r)$, which can be numerically solved imposing again $d\rho/dr(0) = 0$ and $\rho(0) = \rho_0$.

It is possible to follow a different approach, inserting $\rho(r)$ from Eq. (23) into Eq. (15), thus obtaining an equation for $P(r)$. After solving this equation numerically for $P(r)$, $\rho(r)$ can be obtained from Eq. (23). This approach proves to give slightly better results (although similar to the original Kang & He’s) in the fitting procedure, so that is what we used.

4.3 DARKexp

The DARKexp model (Hjorth & Williams 2010; Williams & Hjorth 2010) is significantly different from the previous models, because it does not take into account a possible equation of state to be used in the hydrostatic equilibrium, Eq. (15). Instead, it deals with statistical mechanical arguments to (indirectly) derive the distribution function and determine the density profile.

For the discussion below, let us define a dimensionless density $\tilde{\rho} = \rho/\rho_0$ and a dimensionless distance $x = r/a$, where ρ_0 and a are scale parameters. The particle’s energy per unit mass $E = \Phi + v^2/2$, where Φ is the gravitational potential and v the particle velocity, can be written as

$$\varepsilon = \Phi - \frac{1}{2} \frac{v^2}{v_g^2}, \quad (25)$$

where $v_g = \sqrt{a^2 \rho_0 G}$ and we defined the positive and dimensionless quantities $\varepsilon = -E/v_g^2$ and $\varphi = -\Phi/v_g^2$.

The DARKexp model is based on two main assumptions. First, because dark matter in halos is collisionless, it is argued that, after the system reaches an equilibrium, *each particle* retains its individual energy, and thus a Boltzmann-like function must be used, not in the distribution function $f(\varepsilon)$ (average number of particles

per state of energy ϵ), but in the number of particles per unit energy $N(\epsilon) \propto f(\epsilon)g(\epsilon)$, where $g(\epsilon)$ is the density of states (number of states per unit energy); see Binney (1982). The other feature of the model is that it properly considers the possibility of low occupation numbers, which results in a cutoff similar to that of King models (King 1966; Madsen 1996). These two features imply that the number of particles per unit energy ϵ must be given by

$$N(\epsilon) = e^{\varphi_0 - \epsilon} - 1, \quad (26)$$

where φ_0 is the shape parameter representing the central potential.

In models that predict the distribution function $f(\epsilon)$, the density profile is obtained after integrating over all possible velocities (see Binney & Tremaine 2008)

$$\rho(x) = 4\pi \int dv v^2 \frac{\rho_0}{v_g^3} f(\epsilon), \quad (27)$$

where $f(\epsilon)$ is considered to be dimensionless. The equation above also assumes that the velocities are isotropic, contrary to what is seen in simulated Λ CDM halos (e. g. Lemze et al. 2012) and in observational analysis (e. g. Biviano & Katgert 2004). With the help of Eq. (25), we have

$$\tilde{\rho}(x) = 4\pi \int_0^{\varphi(x)} d\epsilon f(\epsilon) \sqrt{2[\varphi(x) - \epsilon]}. \quad (28)$$

The density profile is finally obtained by solving Poisson's equation

$$\nabla^2 \varphi(x) = -4\pi \tilde{\rho}(x). \quad (29)$$

However, if the model predicts $N(\epsilon)$, as in the case of the DARKexp, we need to use an iterative approach. Here we follow the procedure of Binney (1982). We start by guessing an initial estimate of the density profile $\tilde{\rho}(x)$ and calculate the resulting potential as

$$\varphi(x) = 4\pi \left[\frac{1}{x} \int_0^x dx' x'^2 \tilde{\rho}(x') + \int_x^\infty dx' x' \tilde{\rho}(x') \right]. \quad (30)$$

Next, we compute the density of states as

$$g(E) = (4\pi)^2 \int dr r^2 \int dv v^2 \delta\left(\frac{1}{2}v^2 + \Phi - E\right) \quad (31)$$

which in terms of the dimensionless quantities results in

$$g(\epsilon) = 16\pi^2 a^3 v_g \int_0^{x_{max}(\epsilon)} dx x^2 \sqrt{2[\varphi(x) - \epsilon]}, \quad (32)$$

where x_{max} is such that $\varphi(x_{max}) = \epsilon$. We then use the $N(\epsilon)$ defined in the model, Eq. (26), to compute the dimensionless distribution function

$$f(\epsilon) = a^3 v_g \frac{N(\epsilon)}{g(\epsilon)}. \quad (33)$$

Finally, we use Eq. (28) to obtain a new $\tilde{\rho}(x)$ and iterate the process. We find that after about 20 iterations the model converges to a density profile independent of the initial guess.

Fig. 3 shows the theoretical models described above, after adding to them the 2-halo term explained in §5, along with the galaxy cluster stacked data from Umetsu et al. (2011b).

5 HALO MODEL

When considering cluster profiles that extend to sufficiently large radii, large-scale corrections must be taken into account. For dark matter halos of a given mass M and redshift z , the halo-mass correlation function, defined as $\xi_{hm}(r) = \langle \delta_h(\mathbf{x}) \delta_m(\mathbf{x} + \mathbf{r}) \rangle$, represents

the excess density of matter at a distance $r = |\mathbf{r}|$ from the halo center, i.e. it is a measure of the average observed halo profile $\langle \rho_{obs}(r) \rangle$:

$$1 + \xi_{hm}(r) = \frac{\langle \rho_{obs}(r) \rangle}{\bar{\rho}_m}. \quad (34)$$

The halo model (see Cooray & Sheth 2002) allows us to estimate cosmological correlations from the properties of dark matter halos, seen as the building blocks of cosmic structure. In this context the halo-mass correlation function is given by a sum of two contributions (Hayashi & White 2008; Schmidt et al. 2009)

$$\xi_{hm}(r) = \frac{\rho_{1h}(r)}{\bar{\rho}_m} + b_h^L(M) \xi_m^L(r). \quad (35)$$

Here $\rho_{1h}(r)$ represents the 1-halo contribution or true halo profile from matter within the halo itself; this is the term described by all models presented in §3 and §4. The second term on the right-hand side of Eq. (35) represents the 2-halo contribution from the large-scale structure of the Universe, given by the linear matter correlation function $\xi_m^L(r)$ and the linear halo bias $b_h^L(M)$.

Projected lensing measurements are sensitive to the average observed overdensity $\delta\rho_{obs}(r) = \langle \rho_{obs}(r) \rangle - \bar{\rho}_m$. Therefore, combining Eqs. (34) and (35) we find

$$\delta\rho_{obs}(r) = \rho_{1h}(r) + \rho_{2h}(r), \quad (36)$$

where the 2-halo term is given by

$$\rho_{2h}(r) = \bar{\rho}_m b_h^L(M) \xi_m^L(r). \quad (37)$$

The observed surface density profile $\Sigma_{obs}(R)$ at projected distance R is obtained using Eq. (1):

$$\Sigma_{obs}(R) = \int dx_{||} \delta\rho_{obs}(x_{||}, R) = \Sigma_{1h}(R) + \Sigma_{2h}(R), \quad (38)$$

where $\Sigma_{1h}(R)$ is defined from $\rho_{1h}(r)$, and similarly for $\Sigma_{2h}(R)$. We estimate $b_h^L(M)$ from the fit to simulations of Tinker et al. (2010) and $\xi_m^L(r)$ as the Fourier transform of the linear matter power spectrum $P_m^L(k)$ obtained from CAMB (Lewis, Challinor & Lasenby 2000),

$$\xi_m^L(r) = \frac{1}{2\pi^2} \int dk k^2 P_m^L(k) \frac{\sin(kr)}{kr}. \quad (39)$$

Finally we assume a flat Universe with cosmological parameters $\Omega_m = 0.275$ and $\Omega_\Lambda = 0.725$.

In Fig. 1 we illustrate the effect of the 2-halo term for massive halos. The average redshift of the sample is $z = 0.32$ [see Table (1)]. For this redshift and cosmology, the virial overdensity relative to the mean matter density is $\Delta \approx 263$ (Bryan & Norman 1998). As a first approximation, we fit a NFW profile to the stacked halo data, obtaining a mass $M_{vir} = 1.56 \times 10^{15} M_\odot/h$. With this mass and redshift, the Tinker et al. (2010) fitting formula gives $b_L(M_{263}, z) = 10.98$ for the bias factor, and after calculating the linear matter correlation function we finally obtain the 2-halo term Eq. (37). This is an iterative process, in which the new mass obtained could be used to calculate a new bias factor until it converges, but in this work we restricted the calculation to this first order correction.

Fig. 1 shows that the NFW model underestimates the observed profile for $r > 1$ Mpc/h, where the 2-halo term becomes increasingly important. We add the computed Σ_{2h} to the 1-halo models of §3 and §4 before fitting them to data. Since the 2-halo contribution depends only on the fixed cosmology, this does not introduce any extra parameter.

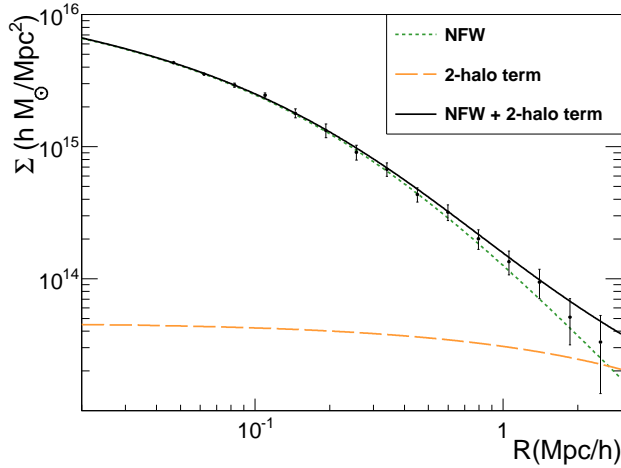


Figure 1. NFW profile (dotted), 2-halo term correction (dashed) and the sum of both (solid) representing the final best fit are shown, along with data points from Umetsu et al. (2011b).

6 RESULTS

We fit the various models to the data with the help of the Minuit package developed by James & Roos (1975). We compute the χ^2 , i.e. the minimum value of Q , given by

$$Q = \Delta_i V_{ij}^{-1} \Delta_j, \quad (40)$$

where

$$\Delta_i = \Sigma_T(R_i) - \Sigma_D(R_i), \quad (41)$$

$\Sigma_T(R_i)$ is the surface density from Eq. (1) for a given model evaluated at radius R_i , $\Sigma_D(R_i)$ is the surface mass density from Umetsu et al. (2011b) lensing analysis of the data, and V_{ij} is the error covariance matrix between data points i and j (see § 2). The data consist of 15 correlated points.

Hereafter, the metric we use to compare the various models is the χ^2 per degree of freedom, or reduced χ^2 , defined as

$$\chi_v^2 = \frac{\chi^2}{\nu} \quad (42)$$

where $\nu = 15 - N_p$ is the number of degrees of freedom given 15 data points and N_p parameters.

We note that a more rigorous statistical analysis would involve the correct calculation of the integral of the χ^2 distribution. Such detailed analysis is beyond the scope of this work, since we are mainly interested in investigating what class of models provide a reasonable description of the data, as inferred from a simple ranking criterion. We believe though that our conclusions would remain unchanged if a more detailed statistical analysis was employed.

Fig. 2 shows the data points obtained by Umetsu et al. (2011b) and the best fits for all the phenomenological models discussed above, after the addition of the 2-halo term represented by the orange dashed line in Fig. 1.

The BMO profile, with 3 parameters and $\chi_v^2 = 0.458$, represents the best fit, with best fit value of the truncation radius given by $\tau = r_t/r_s = 17 \pm 15$. The Stadel profile, with 3 parameters and $\chi_v^2 = 0.465$, represents the second best fit, with best value of the shape parameter $\lambda = 0.25 \pm 0.04$. It is followed by the generalized version of NFW, gNFW (3 parameters), with $\chi_v^2 = 0.471$ and $\alpha = 0.74 \pm 0.44$. Next is the Einasto profile (3 parameters), with $\chi_v^2 = 0.475$ and $n = 3.80 \pm 0.61$. Then we have the Hernquist model

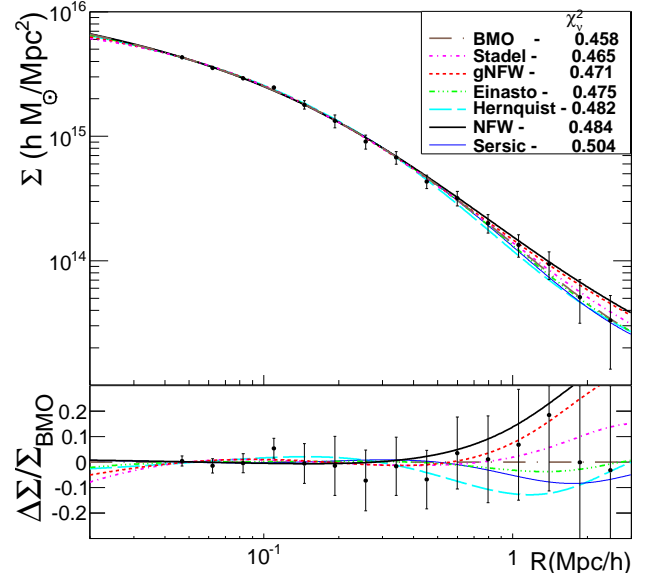


Figure 2. Best fit curves and χ_v^2 for the phenomenological models along with data points from Umetsu et al. (2011b). The bottom panel shows the relative difference between the best fits of each model and the BMO profile.

Profile	N_p	χ_v^2	Shape parameter
BMO	3	0.458	$\tau = 17 \pm 15$
Stadel	3	0.465	$\lambda = 0.25 \pm 0.04$
gNFW	3	0.471	$\alpha = 0.74 \pm 0.44$
Einasto	3	0.475	$n = 3.80 \pm 0.61$
Hernquist	2	0.482	-
NFW	2	0.484	-
Sérsic	3	0.504	$n = 2.42 \pm 0.34$

Table 2. Fit results for the phenomenological models. The column N_p indicates the total number of model parameters, χ_v^2 shows the reduced χ^2 defined in Eq. (42) and the last column shows the best estimate for the shape parameter of the model.

(2 scale parameters) with $\chi_v^2 = 0.482$, followed by the NFW model (2 scale parameters) with $\chi_v^2 = 0.484$. Finally, for the Sérsic profile we obtain $\chi_v^2 = 0.504$ and $n = 2.42 \pm 0.34$. These results are summarized in Table 2.

Fig. 3 shows the fits for the theoretical models. The best fit was obtained for the DARKexp model with $\chi_v^2 = 0.468$. In order to generate this model, we did 25 iterations of the procedure described in § 4.3, with 10^5 logarithmic bins in r . The best fit value for the shape parameter was $\varphi_0 = 3.00 \pm 0.48$. The other three models, the Isothermal Sphere and the 2 variants predicted by Kang & He, were generated in 10^6 logarithmic bins in r .

Among these last three models, the best fit is for the “Kang & He” model, with $\gamma = 3/5$, for which $\chi_v^2 = 2.350$ with $\tilde{\lambda} = \lambda c^2 = (5.44 \pm 0.10) \times 10^4$ and $\tilde{\mu} = \mu (c^3/\rho_0)^{2/5} = 13.85 \pm 0.03$ for the shape parameters, where c is the speed of light in vacuum and ρ_0 is the scale parameter for the density. The Isothermal Sphere gives $\chi_v^2 = 2.603$ and $\tilde{\lambda} = (5.76 \pm 0.16) \times 10^4$ for the shape parameter,

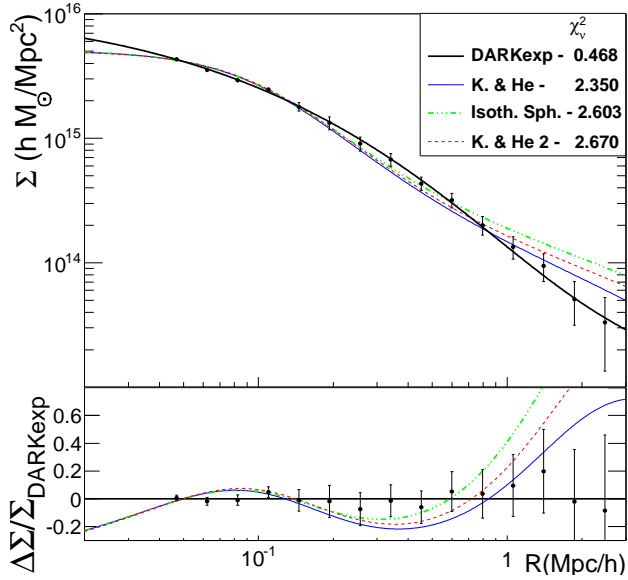


Figure 3. Best fit curves and χ^2_{ν} for the theoretical models, along with data points from Umetsu et al. (2011b). The bottom panel shows the relative difference between the best fits of each model and DARKexp.

Profile	N_p	χ^2_{ν}	Shape parameter
DARKexp	3	0.468	$\varphi_0 = 3.00 \pm 0.48$
KH	4	2.350	$\tilde{\lambda} = (5.44 \pm 0.10) \times 10^4$ $\tilde{\mu} = 13.85 \pm 0.03$
Isoth. Sph.	3	2.603	$\tilde{\lambda} = (5.76 \pm 0.16) \times 10^4$
KH2	4	2.670	$\tilde{\lambda} = (5.29 \pm 0.38) \times 10^4$ $\tilde{\mu} = 346 \pm 268$

Table 3. Fit results for the theoretical models. Columns defined as in Table 2.

followed by “Kang & He 2”, with $\gamma = 4/5$, for which $\chi^2_{\nu} = 2.670$ with $\tilde{\lambda} = (5.29 \pm 0.38) \times 10^4$ and $\tilde{\mu} = \mu (c^8 / \rho_0)^{1/5} = 346 \pm 268$. These results are summarized in Table 3.

6.1 Neglecting the 2-halo term

We have also considered the results of fitting the models without adding the 2-halo term. These fits are summarized in Figs. 4 and 5 and Tables 4 and 5 for the phenomenological and theoretical models respectively.

In this scenario, the NFW profile produces the overall best fit, with $\chi^2_{\nu} = 0.449$ and the gNFW profile results in $\chi^2_{\nu} = 0.474$, with the best fit value $\alpha = 0.89 \pm 0.37$. These values are identical to those obtained by Umetsu et al. (2011b), who did not include the 2-halo term in their analysis, and provides a consistency check of our numerical scheme. The third best fit is the BMO profile with $\chi^2_{\nu} = 0.486$ and $\tau = (3 \pm 124) \times 10^3$ (what in practice makes the model identical to the NFW and shows the complete inadequacy of adding this parameter in this case), followed by Stadel profile with $\chi^2_{\nu} = 0.522$ and $\lambda = 0.223 \pm 0.040$, and by the Einasto profile with $\chi^2_{\nu} = 0.602$ and $n = 4.31 \pm 0.75$. Next, the Sérsic profile resulted in $\chi^2_{\nu} = 0.663$ with $n = 2.69 \pm 0.41$. Finally, for the Hernquist profile,

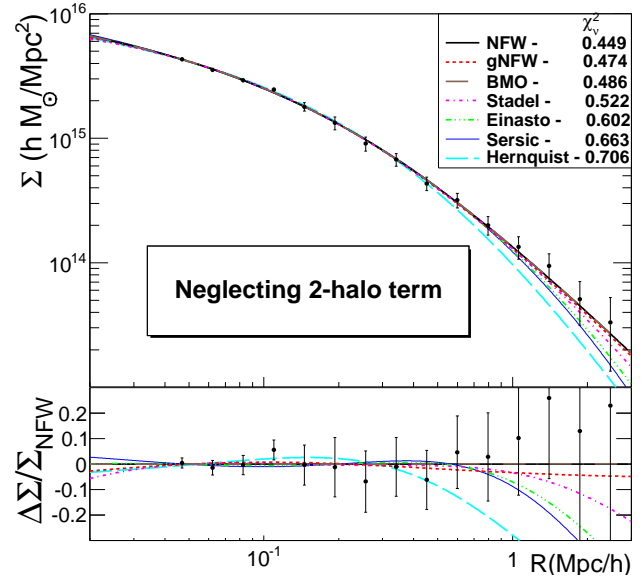


Figure 4. Best fit curves and χ^2_{ν} for the phenomenological models studied, neglecting the 2-halo term, along with data points from Umetsu et al. (2011b). The bottom panel shows the relative difference between the best fits of each model and NFW.

Profile	N_p	χ^2_{ν}	Shape parameter
NFW	2	0.449	-
gNFW	3	0.474	$\alpha = 0.89 \pm 0.37$
BMO	3	0.486	$\tau = (3 \pm 124) \times 10^3$
Stadel	3	0.522	$\lambda = 0.223 \pm 0.04$
Einasto	3	0.602	$n = 4.31 \pm 0.75$
Sérsic	3	0.663	$n = 2.69 \pm 0.41$
Hernquist	2	0.706	-

Table 4. Fit results for the phenomenological models neglecting the 2-halo term. Columns defined as in Table 2.

with 2 scale parameters like NFW, we obtained $\chi^2_{\nu} = 0.706$. These results are summarized in Table 4.

Fig. 5 shows the fits for the theoretical models when we neglect the 2-halo term. The best fit comes from the DARKexp model, for which $\chi^2_{\nu} = 0.598$. The best fit value for the shape parameter was $\varphi_0 = 3.24 \pm 0.48$.

Among the Isothermal Sphere and its variants, the best fit is for the former, which provides $\chi^2_{\nu} = 2.195$ with $\tilde{\lambda} = (5.62 \pm 0.15) \times 10^4$. For the “Kang & He” model, with $\gamma = 3/5$, we find $\chi^2_{\nu} = 2.265$ with $\tilde{\lambda} = (5.477 \pm 0.003) \times 10^4$ and $\tilde{\mu} = 6.1 \pm 0.6$. Finally, for the “Kang & He 2” model with $\gamma = 4/5$, we obtain $\chi^2_{\nu} = 2.385$ with $\tilde{\lambda} = (5.52 \pm 0.36) \times 10^4$ and $\tilde{\mu} = 75 \pm 237$. The results of the fits of these theoretical models are summarized in Table 5.

As can be seen in Figs. 4 and 5, almost all the best fit density profiles remain below the data points in the outer regions. The exceptions are the Isothermal Sphere variants, whose fits nonetheless fail badly. This trend shows the need for including the 2-halo term in the analysis.

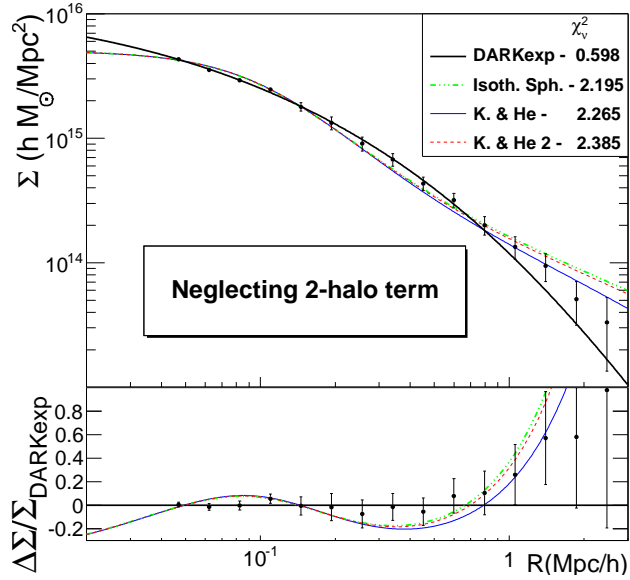


Figure 5. Best fit curves and χ^2_v for the theoretical models studied, neglecting the 2-halo term, along with data points from Umetsu et al. (2011b). The bottom panel shows the relative difference between the best fits of each model and DARKexp model.

Profile	N_p	χ^2_v	Shape parameter
DARKexp	3	0.598	$\phi_0 = 3.24 \pm 0.48$
Isoth. Sph.	3	2.195	$\tilde{\lambda} = (5.62 \pm 0.15) \times 10^4$
KH	4	2.265	$\tilde{\lambda} = (5.477 \pm 0.003) \times 10^4$ $\tilde{\mu} = 6.1 \pm 0.6$
KH2	4	2.385	$\tilde{\lambda} = (5.52 \pm 0.36) \times 10^4$ $\tilde{\mu} = 75 \pm 237$

Table 5. Fit results for the theoretical models neglecting the 2-halo term. Columns defined as in Table 2.

7 DISCUSSION

We have used observed data for the surface mass density of 4 clusters of similar mass and redshift to study various models for cluster density profiles. Under the assumption that the stacked data provide a fair representation of the mean radial density profile of dark matter halos, we can include effects of large-scale structure at large radii and investigate how appropriately each model describes the average properties of clusters of this mass and redshift, and directly compare models against each other.

For the phenomenological profiles, we have found that the BMO model provides the best fit, followed by Stadel, gNFW and Einasto. Nonetheless, the performance of all these profiles, including the standard NFW, is very similar, as is often the case in numerical simulations (Gao et al. 2008; Merritt et al. 2005; Navarro et al. 2010).

For the theoretically motivated profiles, both the Isothermal Sphere and the Kang & He models give poor results compared to the phenomenological models. This can be attributed in part to the fact that both models produce cored density profiles, while the simulations and the data used here favor cuspy profiles, or cored just in

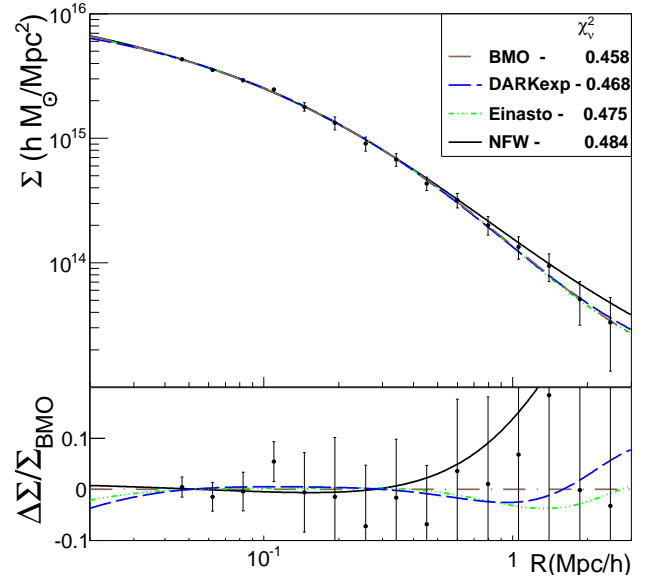


Figure 6. Best fit curves for BMO, DARKexp, Einasto and NFW models, along with data points from Umetsu et al. (2011b). The bottom panel shows differences relative to the BMO profile.

the innermost, inaccessible region, like for the Einasto and Stadel profiles. Moreover, the outer region is not well described by these models, which behave like r^{-2} , while the data favor a behavior closer to r^{-3} .

The best theoretical fit to data is obtained with the DARKexp model. This model provides an excellent fit, even compared with the performance of the phenomenological profiles. This is interesting, since this model has a dynamical basis justification. We did not investigate the role of the velocity anisotropy in this model. However, Williams, Hjorth & Wojtak (2010) have compared the model to simulated data and shown that the typical anisotropy profiles do not alter significantly the predicted density profile and that the DARKexp model is a better match to the Einasto profile than to the NFW profile. This is in agreement with our findings as seen in Fig. 6, which shows our best fits for the BMO, DARKexp, Einasto and NFW profiles.

It is interesting to note that the Einasto profile with $n \approx 6$ generally fits ΛCDM simulations better than NFW, as has been noticed by Navarro et al. (2004). Moreover Mamon, Biviano & Murante (2010) found $n \approx 5$ for dark matter halos of hydrodynamical cosmological simulations, while in this work we have found $n \approx 3.8$. Finally, by fitting rotation curves of spiral galaxies, Chemin, de Blok & Mamon (2011) have found best fits for the Einasto profile with n as low or lower than unity. This sequence may suggest a correlation between the parameter n and the importance of the gas component in the dynamics of the system.

Since the uncertainties, mainly in the external region of the clusters, do not allow us to statistically discriminate between the phenomenological and DARKexp models, we can conclude that the latter represents the data as well as the former but the cored profiles (Isothermal Sphere and its variants) cannot do so.

Regarding the halo model, some cautionary remarks about the methods employed here should be made. We do not expect the simplified halo model considered to describe accurately the transition between 1 and 2-halo terms. It is possible to improve on this prescription by including non-linear effects around the virial radius,

Profile	N_p	χ^2_{ν}	Bias
NFW	3	0.472	3.75 ± 9.14
gNFW	4	0.486	5.71 ± 9.38
Hernquist	3	0.498	15.65 ± 8.75
BMO	4	0.497	13.64 ± 13.10
Stadel	4	0.505	9.45 ± 11.0
Einasto	4	0.511	13.95 ± 10.54
Sérsic	4	0.530	15.73 ± 10.29

Table 6. Fit results for the phenomenological models when the bias is a free parameter. The column N_p indicates the total number of model parameters, χ^2_{ν} shows the reduced χ^2 defined in Eq. (42) and the last column shows the best estimate for the bias.

e.g. by including the non-linear power spectrum and the non-linear cluster bias perturbatively Baldauf et al. (2010). Such a detailed analysis is important to accurately characterize the differences between models in more complete cluster samples, but it is beyond the scope of this work.

In order to roughly access some of the potential degeneracies brought in by non-linear effects, we allow for the linear bias in the 2-halo term to be a free parameter, instead of fixing it to the value from the Tinker et al. (2010) formula. In this case we obtain the constraints shown in Table (6), and the best-fit value for the bias indicates a bit smaller average mass $M_{vir} = 1.52 \times 10^{15} M_{\odot}/h$ for the stacked clusters, again as calculated with the NFW density profile. These results indicate that our best-fits are degenerate with the cluster bias, and likely with parameters describing non-linearities beyond the 1-halo term. Characterizing these non-linear effects precisely and breaking the extra degeneracies induced by them would require a more numerous sample of clusters spanning a larger range in mass and redshift.

Concluding, we find that, while the observed data is best fit by phenomenological models, there is a similarly good fit by the theoretical DARKexp model. We find that including the 2-halo term in the analysis is important and the best-fit ranking somewhat change if it is neglected. Should the agreement with observational data hold for clusters observed at different ranges of mass and redshift, one could argue that theoretical models such as DARKexp may provide a dynamical basis for the observed dark matter density profiles.

ACKNOWLEDGMENTS

We thank Keiichi Umetsu for providing the cluster data and useful comments, Gary Mamon for critical reading of the manuscript and suggestions, Dong-Biao Kang for discussions about features of his models and Liliya L. R. Williams for discussions that helped us reproduce the predictions of the DARKexp model. This work is supported by CNPq, CAPES and FAPESP agencies.

REFERENCES

Alimi J.-M., Bouillot V., Rasera Y., Reverdy V., Corasaniti P.-S., Balmes I., Requena S., Delaruelle X., Richet J.-N., 2012, arXiv:1206.2838

Allen S. W., Schmidt R. W., Fabian A. C., 2002, MNRAS, 334, L11

Baldauf T., Smith R. E., Seljak U., Mandelbaum R., 2010, PRD, 81, 063531

Baltz E. A., Marshall P., Oguri M., 2009, JCAP, 1, 15

Bartelmann M., 1996, A&A, 313, 697

Binney J., 1982, MNRAS, 200, 951

Binney J., Tremaine S., 2008, Galactic Dynamics - Second Edition. Princeton University Press

Biviano A., Katgert P., 2004, AAp, 424, 779

Bosma A., 1978, PhD thesis, Groningen University

Bosma A., van der Kruit P. C., 1979, A&A, 79, 281

Broadhurst T. J., Barkana R., 2008, MNRAS, 390, 1647

Bryan G. L., Norman M. L., 1998, ApJ, 495, 80

Chemin L., de Blok W. J. G., Mamon G. A., 2011, AJ, 142, 109

Ciotti L., 1991, A&A, 249, 99

Clowe D., Bradač M., Gonzalez A. H., Markevitch M., Randall S. W., Jones C., Zaritsky D., 2006, ApJ, 648, L109

Cooray A., Sheth R., 2002, Physics Reports, 372, 1

Einasto J., 1965, Trudy Astrofizicheskogo Instituta Alma-Ata, 5, 87

Eisenstein D. J., Zehavi I., Hogg D. W., Scoccimarro R., Blanton M. R., Nichol R. C., Scranton R., Seo H.-J., Tegmark M., Zheng Z., Anderson S. F., Annis J., Bahcall N., Brinkmann J., Burles S., Castander F. J., Connolly A., et al. 2005, ApJ, 633, 560

Frandsen M. T., Kahlhoefer F., Preston A., Sarkar S., Schmidt-Hoberg K., 2012, JHEP, 2012, 123

Gao L., Navarro J. F., Cole S., Frenk C. S., White S. D. M., Springel V., Jenkins A., Neto A. F., 2008, MNRAS, 387, 536

Gao L., Navarro J. F., Frenk C. S., Jenkins A., Springel V., White S. D. M., 2012, MNRAS, 425, 2169

Hayashi E., White S. D. M., 2008, MNRAS, 388, 2

Hernquist L., 1990, ApJ, 356, 359

Hjorth J., Williams L. R., 2010, ApJ, 722, 851

James F., Roos M., 1975, Computer Physics Communications, 10, 343

Jarosik N., Bennett C. L., Dunkley J., Gold B., Greason M. R., Halpern M., Hill R. S., Hinshaw G., Kogut A., Komatsu E., Larson D., Limon M., et al., 2011, ApJS, 192, 14

Jing Y. P., Suto Y., 2000, ApJ, 529, L69

Kang D.-B., He P., 2011, AAP, 526, A147

Kang D.-B., He P., 2011, MNRAS, 416, 32

King I. R., 1966, The Astronomical Journal, 71, 64

Lapi A., Cavaliere A., 2011, Advances in Astronomy, 2011

Lemze D., Wagner R., Rephaeli Y., Sadeh S., Norman M. L., Barkana R., Broadhurst T., Ford H., Postman M., 2012, ApJ, 752, 141

Lewis A., Challinor A., Lasenby A., 2000, ApJ, 538, 473

Lynden-Bell D., 1967, MNRAS, 136, 101

Madsen J., 1996, MNRAS, 280, 1089

Mamon G. A., Biviano A., Murante G., 2010, AAP, 520, A30

Merritt D., Graham A. W., Moore B., Diemand J., Terzić B., 2006, AJ, 132, 2685

Merritt D., Navarro J. F., Ludlow A., Jenkins A., 2005, ApJ, 624, L85-L88

Mira E. P., Hilbert S., Hartlap J., Schneider P., 2011, A&A, 531, A169

Navarro J. F., Frenk C. S., White S. D. M., 1996, ApJ, 462, 563

Navarro J. F., Frenk C. S., White S. D. M., 1997, ApJ, 490, 493

Navarro J. F., Hayashi E., Power C., Jenkins A. R., Frenk C. S., White S. D. M., Springel V., Stadel J., Quinn T. R., 2004, MNRAS, 349, 1039

- Navarro J. F., Ludlow A., Springel V., Wang J., Vogelsberger M., White S. D. M., Jenkins A., Frenk C. S., Helmi A., 2010, MNRAS, 402, 21–34
- Rubin V. C., Ford W. K. J., Thonnard N., 1980, ApJ, 238, 471
- Rubin V. C., Thonnard N., Ford W. K. J., 1978, ApJ, 225, L107
- Schmidt F., Lima M., Oyaizu H., Hu W., 2009, PRD, 79, 083518
- Sérsic J. L., 1963, Boletín de la Asociación Argentina de Astronomía La Plata Argentina, 6, 41
- Springel V., White S. D. M., Jenkins A., Frenk C. S., Yoshida N., Gao L., Navarro J., Thacker R., Croton D., Helly J., Peacock J. A., Cole S., Thomas P., Couchman H., Evrard A., Colberg J., Pearce F., 2005, Nature, 435, 629
- Stadel J., Potter D., Moore B., Diemand J., Madau P., Zemp M., Kuhlen M., Quilis V., 2009, MNRAS, 398, L21
- Sánchez A. G., Scóccola C. G., Ross A. J., Percival W., Manera M., Montesano F., Mazzalay X., Cuesta A. J., Eisenstein D. J., Kazin E., McBride C. K., Mehta K., Montero-Dorta A. D., Padmanabhan N., Prada F., Rubiño-Martín J. A., et al. 2012, MNRAS, 425, 415
- Taylor J. E., Navarro J. F., 2001, ApJ, 563, 483
- Tinker J. L., Robertson B. E., Kravtsov A. V., Klypin A., Warren M. S., Yepes G., Gottlöber S., 2010, ApJ, 724, 878
- Umetsu K., Broadhurst T., Zitrin A., Medezinski E., Coe D., Postman M., 2011b, ApJ, 738, 41
- Umetsu K., Broadhurst T., Zitrin A., Medezinski E., Hsu L., 2011a, ApJ, 729, 127
- Vikhlinin A., Kravtsov A., Forman W., Jones C., Markevitch M., Murray S. S., Van Speybroeck L., 2006, ApJ, 640, 691
- Williams L. R., Hjorth J., 2010, ApJ, 722, 856
- Williams L. R., Hjorth J., Wojtak R., 2010, ApJ, 725, 282
- Zhao H., 1996, MNRAS, 278, 488
- Zwicky F., 1933, Helv. Phys. Acta, 6, 110